Identification of material properties using indentation test and shape manifold learning approach

Liang Meng, Piotr Breitkopf, Balaji Raghavan, Gerard Mauvoisin, Olivier Bartier, Xavier Hernot

Identification of material properties using indentation test and shape manifold learning approach

L. Meng[a*], P. Breitkopf[a], B. Raghavan[b], G. Mauvoisin[c], O. Bartier[c], X. Hernot[c]

[a] *Sorbonne Universités, Université de Technologie de Compiègne, CNRS Laboratoire Roberval, UMR 7337, Centre de Recherches de Royallieu CS 60319, 60200, Compiègne Cedex, France*

[b] *Laboratoire de Génie Civil et Génie Mécanique EA 3913, INSA de Rennes 20 Avenue des Buttes de Coesmes, 35708 Rennes Cedex, France*

[c] *Laboratoire de Genie Civil et Genie Mecanique EA 3913, Université de Rennes 1, 9 rue Jean Macé, 35000 Rennes, France*

Abstract

The conventional approach for the identification of the work hardening properties of a material by an indentation test usually relies on the force-displacement curve. However, finite element modeling of the indenter-specimen system is a complex task, and the unicity of the solution to the inverse problem of identifying material parameters using the force-displacement curve is not always guaranteed. Also, the precise measurement of the displacement of the indenter tip requires the determination of the indenter frame compliance and indenter tip deformation. To alleviate these problems, we propose in this work an approach based solely on the 3D indentation imprint shape measured after indenter withdrawal, rather than relying on the minimization of the pointwise discrepancy between the experimental and simulated indentation curve. We first build a mathematical "shape space" of indentation shapes in which a lower-dimensional manifold of imprints admissible according to a postulated material constitutive law is approximated. Then, we solve the inverse problem by using a series of predictor-corrector algorithms minimizing the distance between the estimated solution and the experimental imprint in this shape space. We finally apply the proposed approach to indentation tests using a spherical tip indenter on two different materials: a C100 steel specimen and a specimen of the AU4G (AA2017) aluminium alloy.

Keywords: Identification, Shape manifold learning, Indentation test, Reduced Order Modeling

1. Introduction

The identification of material work hardening properties by an indentation test [1, 2] is considered as non-destructive, especially when compared to the tensile test. With the help of indentation tests carried out on different scales, a wide range of materials can be characterized: metals, alloys,

*Corresponding author

Email address: liang.meng@utc.fr (L. Meng[a])

ceramics, concrete [3] or even graded materials[4–8] and the test can also be applied to an actual structure without the need for cutting-out a specimen for tensile testing.
Indentation-based assessment of material properties usually relies on the recorded force-displacement curve (P-h curve) [9–12] obtained in two main phases. In the loading phase, a hard indenter is pressed against the specimen surface. The applied load is increased while the indenter penetrates into the specimen. This phase lasts until the force (or penetration depth) reaches an *a priori* defined value and is followed by removing the indenter from the specimen (unloading phase). The force exerted on the indenter is recorded against the penetration depth over a series of time instants. This P-h curve (Fig.1) is then the primary information used for the identification of material properties. A conventional deterministic identification approach is then applied to minimize the pointwise discrepancy between the simulated and measured P-h curves

$$J_h(\mathbf{c}) = \sum_{i=1}^{N_1} \left(\frac{h_i^s(\mathbf{c}) - h_i^e}{h_{max}^e} \right)^2 , \tag{1}$$

where $\mathbf{c}$ is the vector of material parameters to be identified; h_i is the instantaneous penetration depth of indenter at time instant $i = 1, 2, 3 \cdots N_1$; the superscript 's' refers to 'simulated' by the Finite Element Method (FEM), while the superscript 'e' denotes 'experimental'. Mathematical programming procedures are then used to identify the material properties $\mathbf{c}$ by solving

$$\mathbf{c}^* = Argmin\Big(J_h(\mathbf{c}) \Big). \tag{2}$$

However, nearly identical P-h curves [13, 14] can often be obtained for different materials and

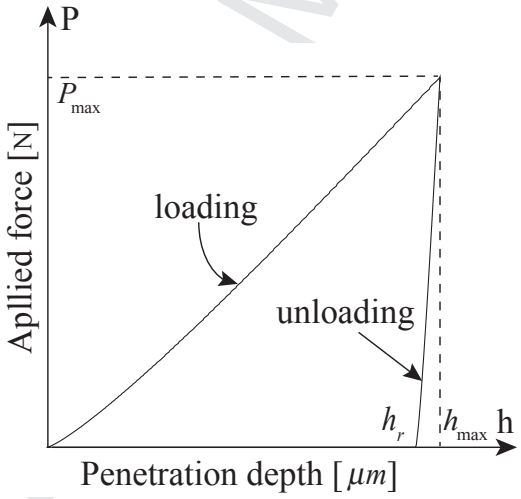

Figure 1: Typical force-displacement (P-h) curve.

this makes the solution to the inverse problem non-unique. Another approach consists in taking into account the residual deformation of the specimen's surface at the conclusion of the indentation test, as additional information to complement the P-h curve [15, 16] since different materials

generally exhibit diverse plastic piling-up (Fig.2) or elastic sink-in effects. A review of existing literature reveals extensive research on combining the traditional indentation test with the mapping of residual deformation (indentation imprint) in order to provide more reliable information for the identification of material properties [4, 17–22]. An atomic force microscope was adopted by [4] to measure the maximum piling-up observed at the end of the test and eventually obtain a well-defined inverse problem for the Al2024 alloy. Imprint mapping was also employed for the identification of bi-dimensional states of stress [22]. This method was later applied to the identification of graded material properties of thin layers on a substrate in [21]. In the inverse problem of property identification using the imprint shape, the cost function J_h in Eq.(1) is replaced by

$$J_u(\mathbf{c}) = \sum_{j=1}^{N_2} \left(\frac{u_j^s(\mathbf{c}) - u_j^e}{u_{max}^e} \right)^2 , \tag{3}$$

where u_j denotes the vertical coordinate of a measured point j with the initial surface of specimen serving as the reference plane; N_2 is the number of sample points chosen from the specimen surface, and this value depends both on the resolution of the imprint scanning instrument and the density of the FE mesh used.

The traditional approach for determination of plastic mechanical properties requires that the in-

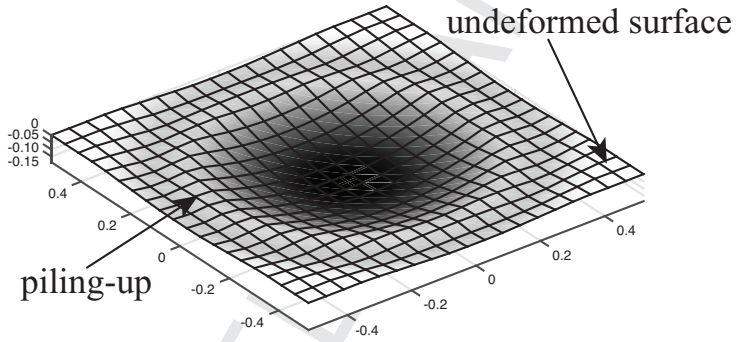

Figure 2: Typical imprint shape.

dentation load/Penetration depth (P-h) response be obtained with sufficient accuracy and precision [23–25]. Two factors that can greatly affect this are the indentation frame/machine compliance and the deformation of the indenter tip. As a result, the behavior of indenter has also been investigated. The indenters were mainly simulated as perfectly rigid bodies to eliminate the nonlinear deformation during the indentation test [26, 27], while [28] corrected a possible elastic deformation of the indenter by a system reduced modulus computed from the Young's modulus and the Poisson's ratio of both the indenter and the specimen. Machine compliance can easily be influenced by tilting or deforming the specimen [24]. The determination of the imprint area, which must be known for the estimation of the machine compliance, is not easy, especially in nanometer scale [25, 29]. Various methods used for the determination of machine compliance can lead to different values of compliance [10]. Presence of compound between the indenter and the indenterholder can lead to a load dependent compliance [24]. An additional difficulty lies in determining the reference

point, or detecting the moment when the indenter comes into contact with the specimen surface. The importance of detecting start point has been pointed out by [30]. It is also recommended to calculate the derivative of the indentation curve in order to limit the effects of a false determination of the zero position [31].

It has been shown that even a small noise in the input data makes the accurate identification of parameters difficult [11, 12]. The indentation curve is observed to be mesh-dependent due to large oscillations with a coarse mesh [32]. A final issue is that the two sources of errors given by $J_h(\mathbf{c})$ and $J_u(\mathbf{c})$ cannot be compared numerically. To alleviate this, [4] proposed calibrating each term by a weighting coefficient so as to render them comparable, however, this approach is somewhat arbitrary. This, then, is an additional argument in favor of solely using the imprint shape in place of the indentation curve.

In the present work, we propose a novel material parameter identification protocol based *only* on the imprint shape of the indentation test using Proper Orthogonal Decomposition [33, 34] and *manifold learning* [35–37]. Following [38, 39], originally applied to the numerical assessment of spring back for the deep drawing process, we build a "shape space" [40] and we apply the concept of shape manifold to describe all the imprint shapes admissible for a postulated constitutive law. The shape manifold is constructed by a series of simulated shape imprints using Design of Experiments (DOE) and POD approach. We then propose a *family of manifold walking algorithms* to determine the search direction in an inverse analysis. Finally, we demonstrate the application of our protocol using an indentation test with a spherical tip indenter on C100 steel and AU4G aluminium alloy.

The remainder of the paper is organized in the following manner: we describe the proposed methodology in detail in Section 2. The Manifold learning algorithms are then presented in Section 3. In Section 4, we apply the protocol to the identification of material hardening parameters of the C100 steel, using the actual experimental indentation imprint obtained by using the Chromatic Confocal Imaging technique. A detailed discussion is also made at the end of this section to demonstrate the robustness of the proposed method with respect to the number of retained modes, order of polynomial basis as well as number of snapshots. In Section 5, the hardening properties of a specimen of AU4G alloy is also studied, in which the experimental imprint is measured with bigger noise. The paper ends with concluding comments and suggestions for future work.

2. Basic Approach

We first consider the numerical simulation of an axisymmetric indentation test on a specimen using a spherical tip indenter. The typical FE model and the residual deformation of the specimen are shown in Fig.3. The imprint shape obtained by simulation using the above FE model is characterized by the vertical displacements of the surface nodes of the specimen, stored in a vector $\mathbf{s} \in \Re^n$, where n is the number of surface nodes of the mesh in the domain of interest. The identification of the material properties then aims at finding a material properties set $\mathbf{c}^* = (c_1, c_2 \cdots c_l)$ (l is the number of parameters identified), which minimizes the error between the simulated and experimental imprint. The fundamental hypothesis of our method is that the set of all possible imprint shapes governed by a postulated constitutive law forms a smooth manifold in some m-dimensional space ($m \ll n$). The identification of material properties will be then carried out in

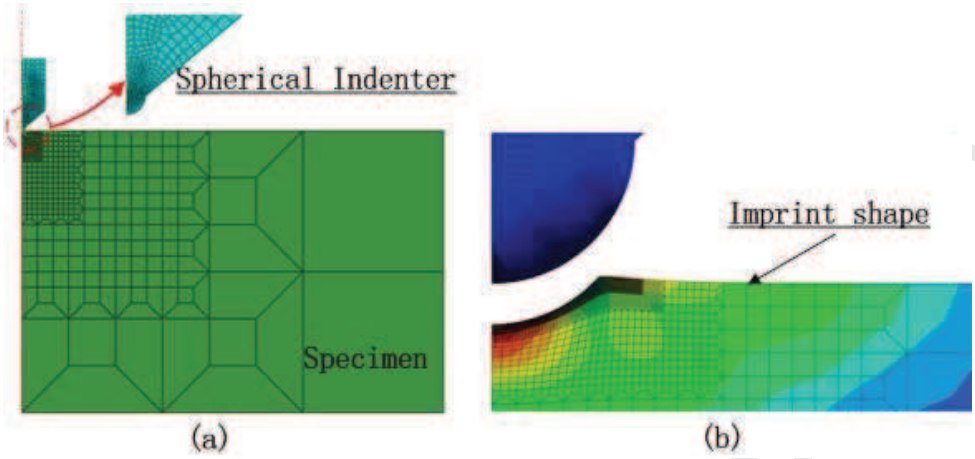

Figure 3: FE simulation model of indentation test and residual displacement of the specimen.

this lower-dimensional space. We propose to approximate this space by successive applications of DOE and POD.

2.1. Construction of the shape space

We begin with M numerical experiments defined by an appropriate DOE for the varying set of design parameters $\mathbf{c}^{(i)}, i = 1, 2 \cdots M$ representing the material parameters to be identified. Different imprint shapes $\mathbf{s}^{(i)} = \mathbf{s}(\mathbf{c}^{(i)})$ extracted from the numerical simulation results are then considered as *imprint snapshots* (Fig.4). The centered snapshot matrix $\mathbf{S}$ is given by

$$\mathbf{S} = [\mathbf{s}^{(1)} - \bar{\mathbf{s}}, \mathbf{s}^{(2)} - \bar{\mathbf{s}}, \cdots \mathbf{s}^{(M)} - \bar{\mathbf{s}}], \tag{4}$$

where $\bar{\mathbf{s}}$ is the mean snapshot

$$\bar{\mathbf{s}} = \frac{1}{M} \sum_{i=1}^{M} \mathbf{s}^{(i)}. \tag{5}$$

Singular value decomposition [41] of $\mathbf{S}$ yields

$$\mathbf{S} = \mathbf{\Phi D V^T}, \tag{6}$$

where the diagonal matrix $\mathbf{D}$ contains the singular values $d_i, i = 1, 2 \cdots M$; each column of $\mathbf{\Phi} = [\boldsymbol{\phi}^{(1)}, \boldsymbol{\phi}^{(2)} \cdots \boldsymbol{\phi}^{(M)}]$ is an eigenvector of the covariance matrix $\mathbf{C} = \mathbf{S S^T}$. The eigenvectors $\boldsymbol{\phi}^{(i)}$ are also called the i^{th} POD modes. Fig.5 gives the mean of all snapshots from Fig.4 and the modes scaled by the corresponding eigenvalues $\lambda_i = d_i^2$. Each snapshot $\mathbf{s}^{(i)}$ can then be accurately reconstructed by

$$\mathbf{s}^{(i)} = \bar{\mathbf{s}} + \mathbf{\Phi} \boldsymbol{\alpha}^{(i)} = \bar{\mathbf{s}} + \sum_{j=1}^{M} \alpha_j^{(i)} \boldsymbol{\phi}^{(j)}, \tag{7}$$

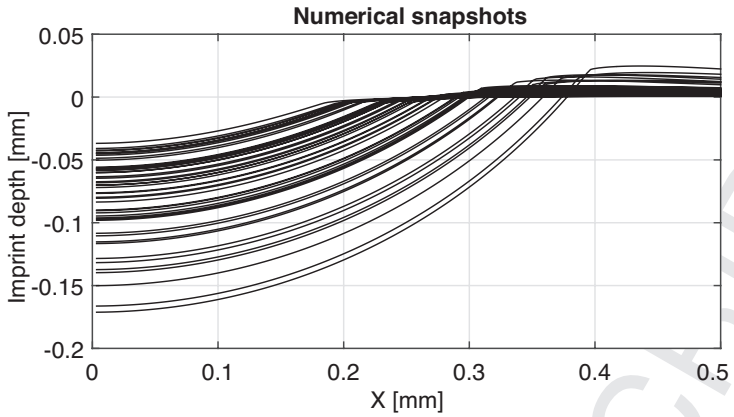

Figure 4: A series of snapshots obtained for varying material parameters.

where $\alpha_j^{(i)}$ is the projection coefficient for the i^{th} snapshot on the j^{th} mode

$$\alpha_j^{(i)} = \left(\boldsymbol{\phi}^{(j)}\right)^{\mathbf{T}}\left(\mathbf{s}^{(i)} - \bar{\mathbf{s}}\right), j = 1, 2 \cdots M. \tag{8}$$

At this point, we build such a shape space, the origin of which is the mean snapshot and the POD modes serve as the orthogonal basis. Consequently, each imprint snapshot can be described by its coordinates in alpha space $\boldsymbol{\alpha}^{(i)}, i = 1, 2 \cdots M$ by Eq.(8).
In standard POD, one considers only $m \ll M$ significant modes corresponding to the biggest eigenvalues of the covariance matrix by referring to the following criterion

$$\epsilon = 1 - \frac{\sum_{i=1}^{m} \lambda_i}{\sum_{j=1}^{M} \lambda_j}. \tag{9}$$

and by fixing a threshold for ϵ. However, the difficulty lies in the choice of a proper value for ϵ. Here, instead of reducing the number of modes, we exploit the concept of the $\alpha-$manifold and analyze the dependence of projection coefficients α_i with respect to the material parameters $c_j, j = 1, 2 \cdots l$

$$\alpha_i = \alpha_i(c_1, c_2 \cdots c_l), i = 1, 2 \cdots M. \tag{10}$$

Thus, we may use all the modes without truncation i.e. $m = M$. In this case, the approximation of the imprint shape depending only on the l constitutive parameters but not on the number of modes

$$\tilde{\mathbf{s}}^{(i)} = \bar{\mathbf{s}} + \sum_{j=1}^{m=M} \alpha_j^{(i)}(c_1, c_2 \cdots c_l)\boldsymbol{\phi}^{(j)}. \tag{11}$$

In the cases where the simulated imprints are already orthogonal, we will keep all the modes, but the approximation in Eq.(11) will still depend only on $l < M$ parameters. However, in most cases, the reduction of the number of modes is still possible, and the effect of adopting different numbers of modes is analyzed in Section 4.3.1.

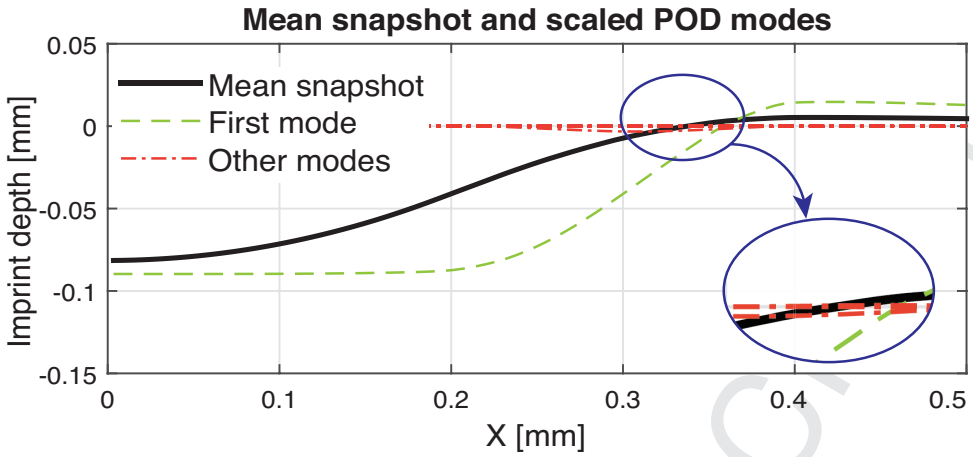

Figure 5: The mean snapshot and different POD modes scaled by the corresponding eigenvalues.

2.2. *Manifold $\mathcal{M}$ of admissible shapes*

For a set of M simulated imprint shapes, Eq.(8) gives their coordinates $\boldsymbol{\alpha}^{(1)}$, $\boldsymbol{\alpha}^{(2)}$ $\cdots$ $\boldsymbol{\alpha}^{(M)}$ in α-space. We recall the fundamental assumption that all imprint shapes admissible with a given material law lie on a smooth manifold

$$\mathcal{M}(\boldsymbol{\alpha}) = 0. \tag{12}$$

We use a parametric representation of $\mathcal{M}$

$$\alpha_i(\mathbf{c}) = \boldsymbol{p}^{\mathbf{T}}(\mathbf{c})\boldsymbol{a}^{(i)}, i = 1, 2 \cdots M, \tag{13}$$

with polynomial basis $\boldsymbol{p}$ and the coefficient vectors $\boldsymbol{a}^{(i)}$ approximated for all $\alpha_i^{(j)}$, $j = 1, 2 \cdots M$ by minimizing least-square error

$$\boldsymbol{a}^{(i)} = Argmin \frac{1}{2} \sum_{j=1}^{M} \left(\boldsymbol{p}^{\mathbf{T}}(\mathbf{c}^{(j)})\boldsymbol{a}^{(i)} - \alpha_i^{(j)} \right)^2. \tag{14}$$

For each point in the design space defined by the constitutive parameter values, we can find a corresponding point on the manifold by using Eq.(13). On the contrary, each point on the manifold corresponds to an imprint snapshot and, by consequence, also to a set of parameter values in design space. Thus a one-to-one relationship is built up between the design space and the shape manifold in α-space (Fig.6). For the purpose of visualization, only a 3D section of the higher-dimensional space is presented.

2.3. *Identification of material properties*

The goal of the identification procedure is then simply to minimize the distance between the simulated and experimental imprint ($\mathbf{s}_{exp}$) shapes in α-space. The projection of the experimental

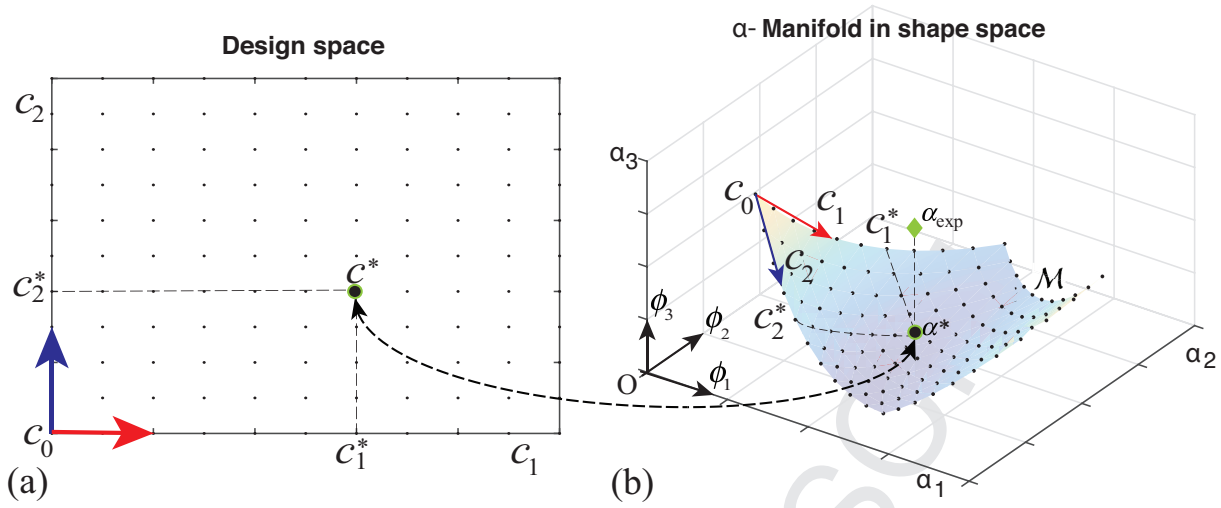

Figure 6: (a) Design space (b) Shape manifold $\mathcal{M}$ in α-space.

imprint $\tilde{\mathbf{s}}_{exp}$ is

$$\tilde{\mathbf{s}}_{exp} = \bar{\mathbf{s}} + \mathbf{\Phi}\mathbf{\Phi}^{\mathbf{T}}(\mathbf{s}_{exp} - \bar{\mathbf{s}}) = \bar{\mathbf{s}} + \mathbf{\Phi}\boldsymbol{\alpha}_{exp}, \tag{15}$$

and it is represented by the coordinates $\boldsymbol{\alpha}_{exp}$ in shape space. When comparing $\tilde{\mathbf{s}}_{exp}$ with the experimental imprint $\mathbf{s}_{exp}$ (Fig.7), we note that the measurement noise is smoothed out by linear combinations of smooth POD modes. The projection of the experimental imprint in α-space may be thus be considered as a physics-based smoothing procedure.

According to the fundamental hypothesis used in this paper, even assuming that the indented material behaves exactly according to the postulated hardening law, the projection $\boldsymbol{\alpha}_{exp}$ will not lie on the global manifold $\mathcal{M}$ (Fig.6). In this case, noise in measurement is the only reason for the offset of the experimental imprint from the shape manifold. In the implementation of our method, however, except for the measurement noise, there is an additional factor: the inaccuracy of local manifold (since it is merely a lower order approximation of the global manifold). Generally, in current work, since the manifold is being approximated in the vicinity of the snapshot, and considering the simplicity of the problem itself (only two parameters are involved, so the manifold will not be particularly complex), we hold the idea that the error caused by measurement noise must be dominant compared with that incurred by manifold inaccuracy. Thus, ignoring the inaccuracy of local manifold, our goal is to find the closest point $\boldsymbol{\alpha}^*$ on $\mathcal{M}$ such that

$$\mathbf{c}^* = Argmin||(\boldsymbol{\alpha}_{\text{exp}} - \boldsymbol{\alpha}(\mathbf{c}))||, \alpha(\mathbf{c}) \in \mathcal{M}. \tag{16}$$

Therefore, the identification of material properties can be carried out in at most an M-dimensional space. We recall that $M \ll n$, where n is the dimensionality of the imprint shape vector $\boldsymbol{s}$ used in Eq.(4). Taking into account Eq.(7) and (15), we note that the convergence criterion in Eq.(16) is equivalent to

$$\mathbf{s}^* = \mathbf{s}(\mathbf{c}^*) = \underset{\mathbf{s}}{\text{Argmin}}||\tilde{\mathbf{s}}_{\text{exp}} - \mathbf{s}(\mathbf{c})||. \tag{17}$$

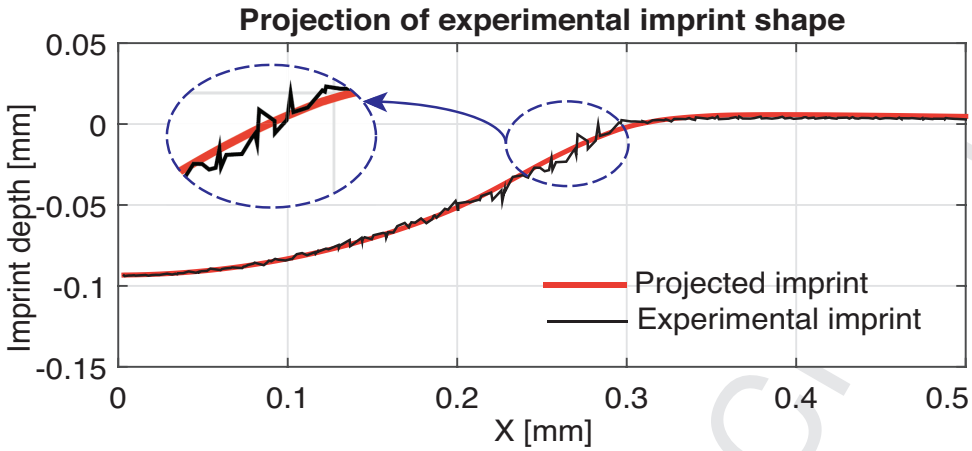

Figure 7: Projection of an experimental imprint to α-space.

We summarize the steps involved in our shape manifold-based identification in α-space as follows:

- Construct a shape space using an appropriate DOE;
- Project real experimental imprint shape into the shape space;
- On the manifold, find the coordinates of closet point to the experimental projection;
- Derive the material parameters in design space.

Note that, the identification is performed in the $\alpha-$ space, and the procedure does not depend on the number of retained modes m, but it depends on the intrinsic dimensionality $d \leq l$ of the manifold.

3. Algorithm families

According to the fundamental hypothesis our current work is based on, a *global manifold* is defined as a smooth hyper surface that connects *all* the imprint shapes admissible according to the postulated constitutive law. Therefore, simply projecting the experimental imprint on the global $\alpha-$manifold and finding the closest point to the experimental snapshot will lead to the desired solution. However, this would demand extensive off-line simulations in most cases simply to construct with sufficient accuracy a global manifold for identification, since it is always high-dimensional and nonlinear. In the present work, we propose an *on-line* approach which constructs only the *useful* portion of $\mathcal{M}$ (local manifold) progressively by using the predictor-corrector strategy issued from our former work [38, 39]. Thus the manifold is represented by a series of local polynomials. For illustration purposes, we adopt a global two-parameter-design space and a local design window, with the width and height referring to the range of variation of the two parameters at current iteration.

3.1. panning

In this algorithm, the design window pans in the whole design space while the window size remains unchanged (Fig.8). For the sake of clarity, only the snapshot located at the center of each

DOE is depicted. For the first iteration step, we calculate a prediction with the initial design window. If the new prediction lies outside of this window, we limit it to the window boundary and the next iteration window will be centered around this new prediction. We repeat this process until the prediction is positioned in the current window and the convergence criterion in Eq.(16) is satisfied.

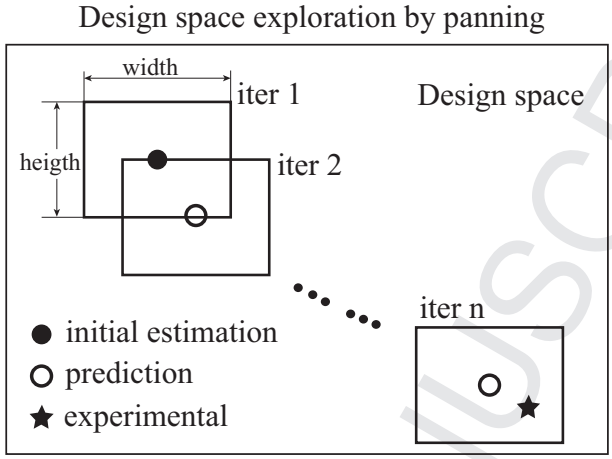

Figure 8: Panning iterations.

3.2. zooming

In this algorithm, the first design of experiments covers the entire design space, after which the window size is cut down with each subsequent iteration, as shown in Fig.9. Similar to the panning algorithm, a new prediction is first computed with the current design window. We center the new design window (of smaller size) around the estimate. This process is repeated until convergence.

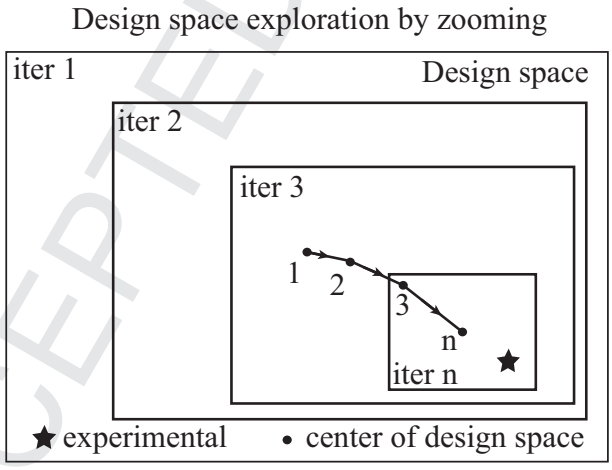

Figure 9: Zooming iterations.

3.3. panning & zooming

The panning & zooming method essentially combines both of the previous approaches. As illustrated in Fig.10, the general idea behind this algorithm is the use of a panning search at the beginning until the estimate for the next iteration lies inside the current design space instead of on the boundary, after which the search scheme will be switched to zooming in order to improve the accuracy of the local manifold.

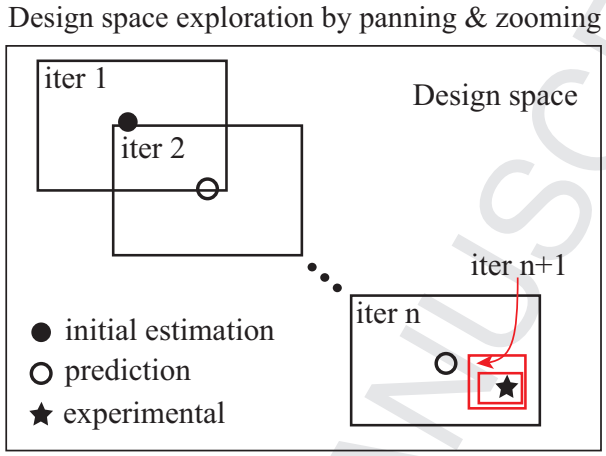

Figure 10: Combination of zooming and panning.

4. MAIN TEST CASE: C100 STEEL

4.1. Problem description

The methodology proposed in the previous sections was verified by an axisymmetric indentation test on C100 steel using a spherical tip indenter with a radius of 0.5 *mm*. This kind of indenter does not give a useful P-h curve on account of the presence of compound between the indenter and indenter holder, and thus the authors felt that it was a good candidate for our imprint-based identification protocol. The material was chosen for its homogeneous micro-structure, which ensures the reproducibility of the indentation test. The specimen was carefully sectioned and polished using fine emery papers (up to 1200 grit) and diamond suspensions (6 and 3 μm) in order to avoid uncertainties due to roughness. The experimental (real) imprint shape was obtained using a metrological machine Altisurf 500 based on the optical principle of chromatic confocal imaging.
A power Hollomon's law is employed for the isotropic hardening of our test case since it is a good approximation for most metals and alloys [42]. This law describes the relationship between the equivalent stress and the plastic strain, while the elastic portion follows Hooke's law. The continuity of the stress-strain curve at the elastic limit is enforced, resulting in

$$\sigma = \sigma_y \left(\frac{E}{\sigma_y} \right)^n \varepsilon^n, \tag{18}$$

where σ is the equivalent stress, and ε refers to the total strain. The behavior law of the material is thus described by three parameters: yield stress σ_y, strain hardening exponent n and Young's modulus E. E is fixed at 21000MPa and Poisson's ratio ν is fixed at 0.3, while two other parameters that control the plastic properties will be identified. Even if we already have a general estimation for the properties of the above-mentioned material ($\sigma_y \approx 100Mpa$, $n \approx 0.3$), the parameters are identified in a large design space ($n \in [0.1, 0.5]$, $\sigma_y \in [50, 400]$) so as to keep the material of interest away from the boundaries [43]. This will ensure the accuracy during the inverse analysis and allow to test the robustness of the proposed methodology.
The numerical simulation of the indenter test is carried out within the commercial software ABAQUS [44] by using the FE model in Fig.3. Four-noded axisymmetric elements (CAX4) were used with 4394 elements for the specimen and 6070 elements for the indenter. The contact interface between the indenter and the specimen was characterized by a Coulomb friction coefficient of 0.1. The indentation force is progressively increased up to a prescribed value ($F_{max} = 500N$) and the unloading phase is simulated in one step, resulting in a final imprint shape after spring back.
Due to the axisymmetric property of the model, the imprint shape (simulated) was obtained by extracting the vertical displacements of sample points on half of the imprint, while the experimental indentation imprint shape was voxelized using a resolution of 200×200 by scanning the vicinity of the center of the imprint. The step length along each direction was 10 μm which rests with the resolution of the scanning machine.

4.2. Results and discussion

Three manifold learning algorithms are used for the resolution of identification problem of this test case. A quadric polynomial basis (2D), containing 6 different terms, was applied for the construction of the smooth manifold in Eq.(13). 7 snapshots were chosen in each DOE using Latin Hyper Cubic sampling. These snapshots were then decomposed using POD with a full basis of size 7, giving a set of $\alpha_1, \alpha_2 \cdots \alpha_7$ for each of the 7 snapshots. In the present work, we have used a full basis without truncation, leading to a $7-dimensional$ shape space. For the purpose of visualization, only the first three coordinates were chosen. We identify two plastic parameters of C100 in this mathematical space by using the convergence criterion given in Eq.(16). The error in identification by comparing the physical and simulated imprint shapes is calculated by

$$\varepsilon_1 = \frac{||\tilde{\mathbf{s}}_{\text{exp}} - \mathbf{s}(\sigma_y, n)||}{||\tilde{\mathbf{s}}_{\text{exp}}||}. \tag{19}$$

In order to demonstrate the advantage of using this adaptive mathematical shape manifold, we have also calculated the error between the imprint shape obtained by simulation using the identified parameters and the real experimental data

$$\varepsilon_2 = \frac{||\mathbf{s}_{exp} - \mathbf{s}(\sigma_y, n)||}{||\mathbf{s}_{\text{exp}}||}. \tag{20}$$

4.2.1. panning

Table 1: Iteration results using panning approach.

Iter	σ_y	n	$\Delta\sigma_y$	Δn	$\|\boldsymbol{\alpha}_{\text{exp}} - \boldsymbol{\alpha}^*\|$	ε_1	ε_2
1	205.0	0.225	30	0.05	0.0629	8.01%	8.78%
2	190.1	0.226	30	0.05	0.0327	4.15%	5.56%
3	175.1	0.239	30	0.05	0.0292	3.71%	5.16%
4	160.1	0.260	30	0.05	0.0219	2.79%	4.57%
5	145.1	0.275	30	0.05	0.0171	2.18%	4.20%
6	130.2	0.294	30	0.05	0.0118	1.50%	3.88%
7	115.4	0.312	30	0.05	0.0052	0.66%	3.58%
8	104.0	0.330	30	0.05	0.0030	0.38%	3.53%

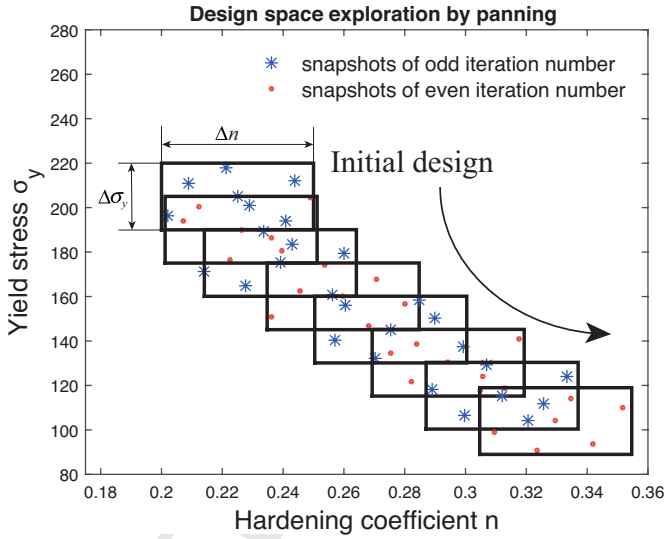

Figure 11: Panning iterations (Table.1).

The iteration history for identification using the panning algorithm is given in Table.1. Design of experiments is centered around successive sets of σ_y and n. $\Delta\sigma_y$ and Δn are the size of the design window. The pattern of exploration of the total design space by panning the design window is shown in Fig.11. Different symbols are used for odd and even iteration numbers for clearer visualization. For overlapping windows, the snapshots can be reused in order to save computing time.

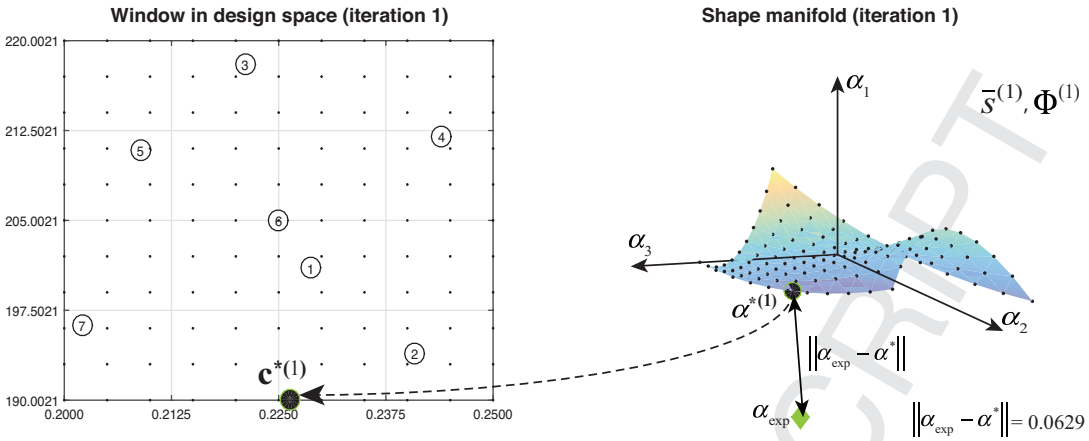

Figure 12: Material parameters identification procedure by design space and local manifold 1 in α-space.

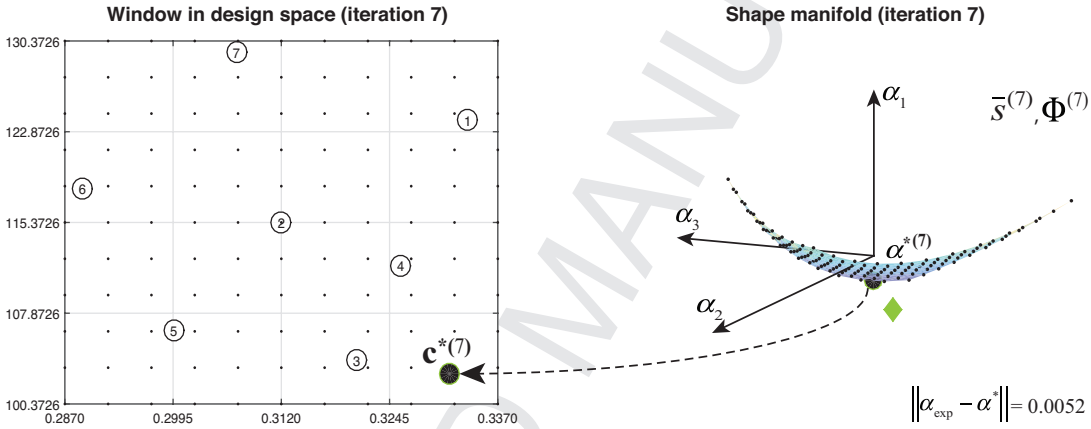

Figure 13: Material parameters identification procedure by design space and local manifold 7 in α-space.

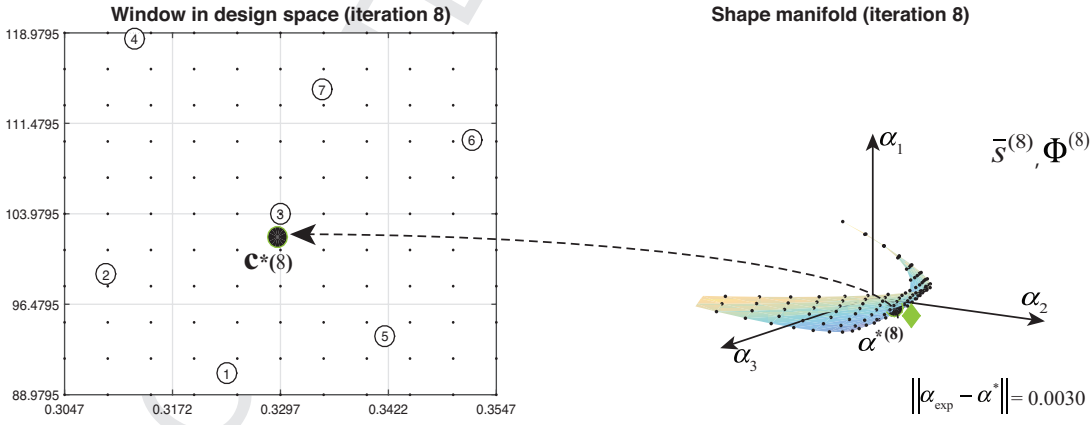

Figure 14: Material parameters identification procedure by design space and local manifold 8 in α-space.

Successive design spaces and corresponding local manifolds are shown in Fig.12-14. The green diamond, referring to the projection of experiment imprint in α-space, converges to the center of the local coordinate system, which also implies that the estimated imprint convergences to $\mathbf{s}_{exp}$. The black dot in design space represents the current estimation parameters corresponding to the point on $\mathcal{M}$ closest to the projection of experimental imprint. The local manifolds in this panning method are not accurately approximated for the simple reason that we are using only a quadric surface to approximate $\mathcal{M}$ in a relatively wide range($\Delta\sigma_y = 30, \Delta n = 0.05$). With the panning method, we can only obtain a general estimate for the material parameters. The accuracy can be improved by either increasing the degree of polynomial basis or by shrinking the size of the window.

Table 2: Iteration results using regular zooming approach.

Iter	σ_y	n	$\Delta\sigma_y$	Δn	$\|\boldsymbol{\alpha}_{\text{exp}} - \boldsymbol{\alpha}^*\|$	ε_1	ε_2
1	250.0	0.250	320	0.3	0.2512	31.97%	32.16%
2	99.79	0.394	160	0.15	0.0155	1.97%	4.25%
3	98.32	0.336	80	0.08	0.0150	1.90%	3.89%
4	98.65	0.331	40	0.04	0.0056	0.71%	3.59%
5	112.44	0.327	20	0.02	0.0147	1.87%	3.57%
6	105.80	0.326	10	0.01	0.0092	1.16%	3.54%
7	105.46	0.326	5	0.005	0.0079	1.01%	3.57%
8	105.79	0.326	2.5	0.002	0.0069	0.87%	3.57%

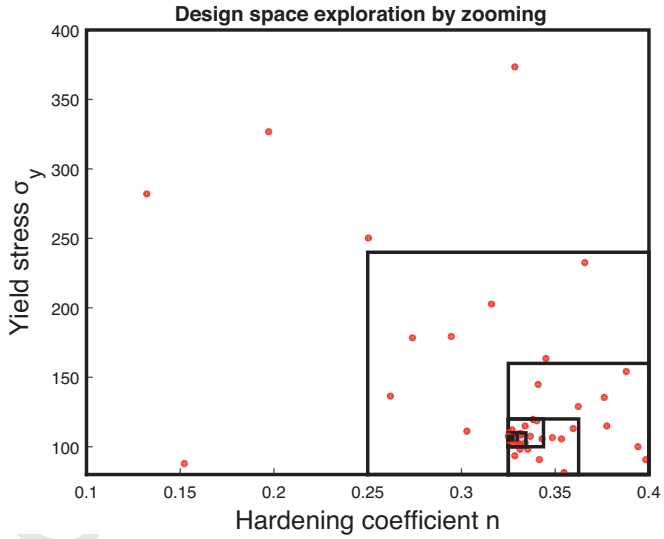

Figure 15: Zooming steps (Table.2).

4.2.2. zooming

For this algorithm,the convergence of the material properties is shown in Table.2, where σ_y stabilized around 105 and n around 0.326. Clearly, the standard error ε_2 has stabilized at 3.6% after only 3 iteration steps, while the proposed error ε_1 drops to around 1% by using the projected imprint in shape space. Even the error ε_1 in the 4^{th} iteration is smaller than the last one, we still prefer the material identified in the last step for the reason that the local manifold is more accurate so as to obtain the projection of the experimental imprint. The last manifold is considered accurate since the identification is carried out in a small window size and the material parameters vary only in a small range: 2.5 for σ_y and 0.002 for n. The iteration procedure in design space is shown in Fig.15. Also, imprint snapshots at various stages and the experimental imprint are compared (Fig.16). It is clear that the simulated imprint shapes will concentrate around the experimental one when the local manifold patch decreases in size along with subsequent iterations.

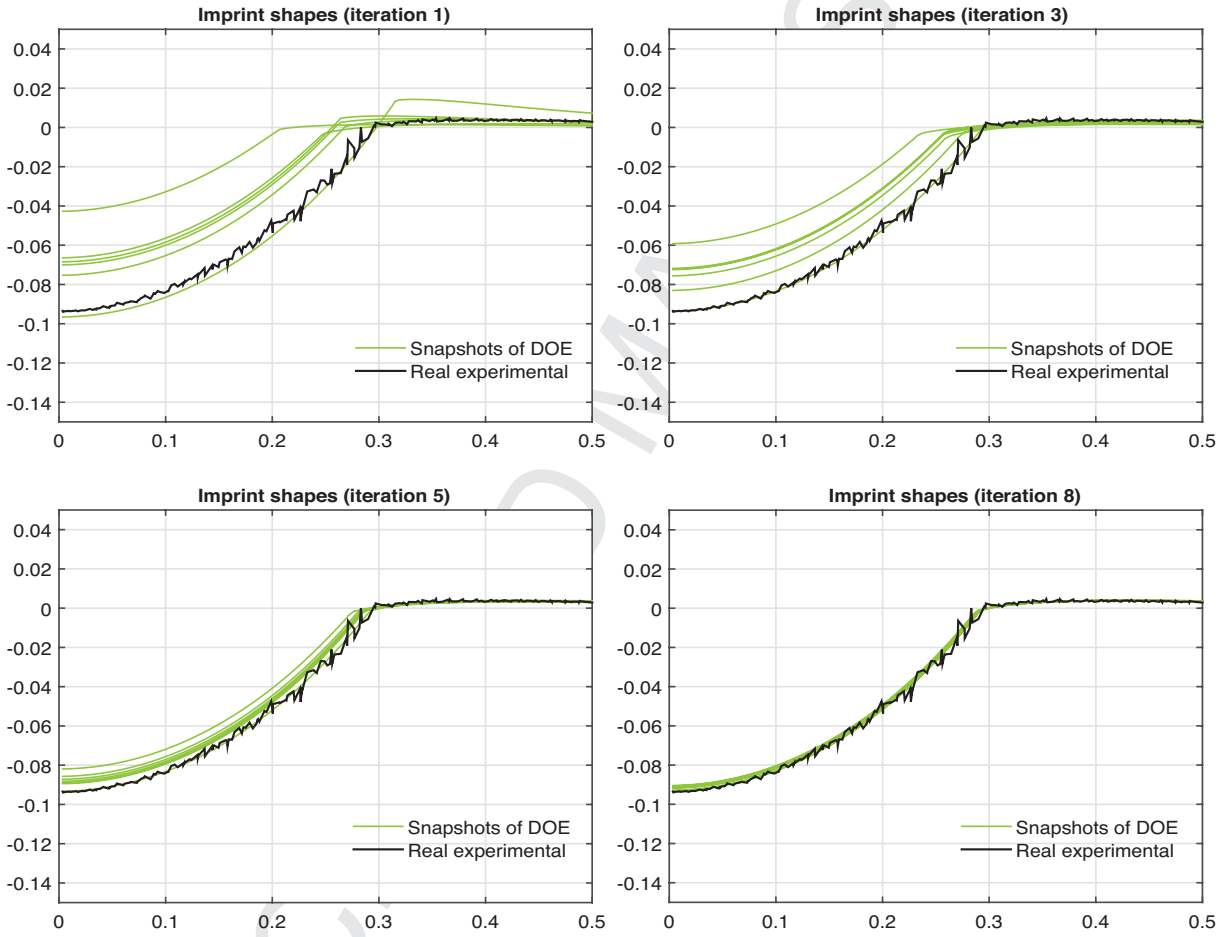

Figure 16: Experimental imprint and numerical snapshots (zooming algorithm).

4.2.3. panning & zooming

Finally, a combined algorithm of panning and zooming is applied. A similar estimation of material properties is obtained (Table.3). In the first four steps, the panning method is introduced to iteratively locate the most promising zone, and during these steps the design window remains the same size. Next, the zooming algorithm is adopted in order to improve the accuracy of the local manifold for better identification. The first searching algorithm is automatically switched to the second one as soon as the estimate for the next iteration is located inside the current design space rather than on the boundary. The pattern of exploration in design space is visualized in Fig.17.

Table 3: Iteration results using panning & zooming.

Iter	σ_y	n	$\Delta\sigma_y$	Δn	$\|\alpha_{\text{exp}} - \alpha^*\|$	ε_1	ε_2
1	175.0	0.300	40	0.04	0.1989	25.31%	25.56%
2	155.0	0.280	40	0.04	0.0697	8.87%	9.62%
3	135.2	0.287	40	0.04	0.0175	2.22%	3.98 %
4	120.5	0.307	40	0.04	0.0083	1.05%	3.68%
5	107.0	0.326	20	0.02	0.0059	0.75%	3.54%
6	108.0	0.323	10	0.01	0.0121	1.53%	3.57%
7	106.7	0.323	5	0.005	0.0089	1.13%	3.56%
8	107.0	0.324	2.5	0.002	0.0096	1.22%	3.57%

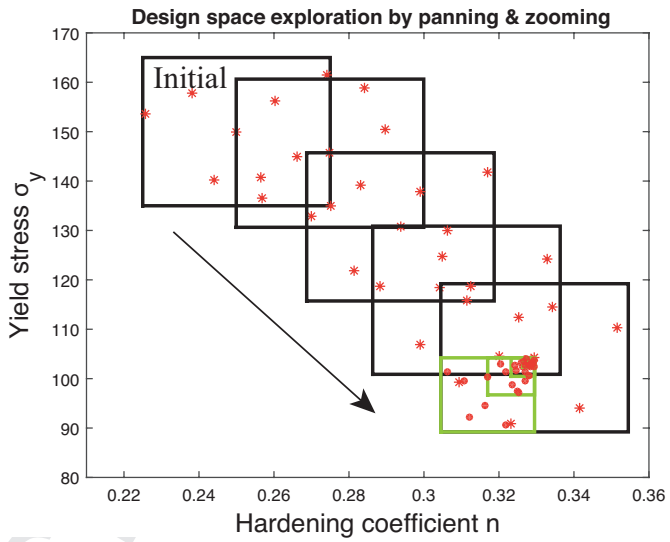

Figure 17: Combination of zooming and panning (Table.3).

4.2.4. Comparison of three methods

For the purpose of comparison, the convergence patterns of material parameters identified by the three different algorithms are depicted in Fig.18. The robustness of the identification procedure

in lower-dimensional $\alpha-$space is confirmed by using different initial points for the three algorithms which lead to identical material parameters. In addition, it may also be concluded from the iteration histories that the combined zooming & panning approach gives the best convergence of *both* parameters. Therefore, In the following section, we retain the panning & zooming algorithm.
The identification error ε_1 is shown in Fig.19. Obvious decreases are observed, and these stabilize at around 1%. It is worth mentioning that this error is more reliable if the design space is smaller for each iteration step. That's why we prefer the result in the 8^{th} iteration to that in the 4^{th} iteration in Table.2.

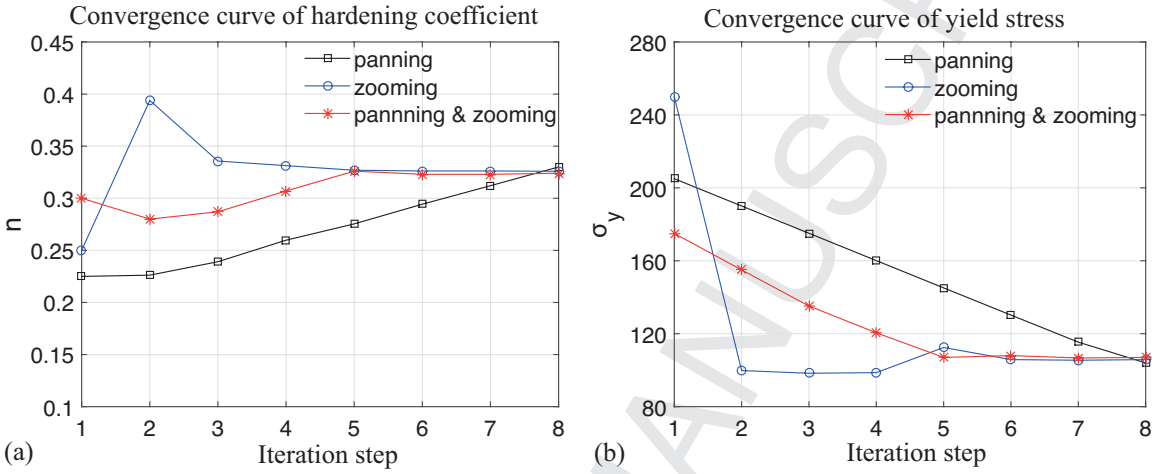

Figure 18: Convergence patterns for the parametric identification of n and σ_y.

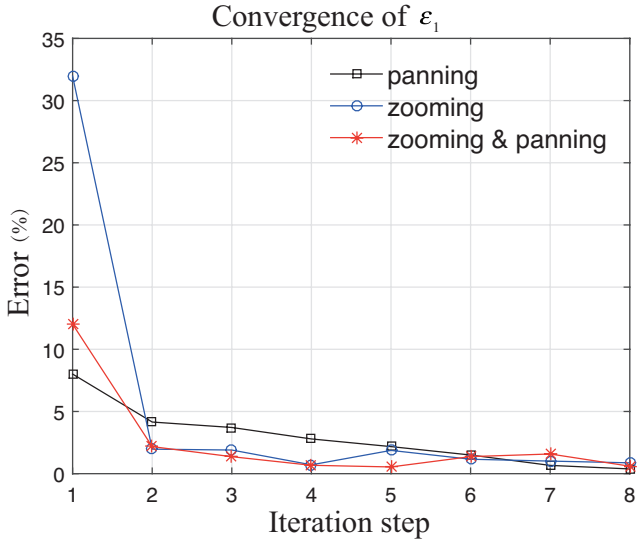

Figure 19: Progressive reduction of the error estimation function ε_1 between the imprint shape obtained with identified parameters and the reconstructed experimental imprint with POD modes.

4.3. Verification of robustness

4.3.1. Truncation on POD modes

In our work, we aim to minimize the distance between the experimental and simulated imprints in shape space. Thus, it is unnecessary to perform any truncation like in the traditional POD method. First of all, the optimization problem is already placed in a rather low dimensional space, and computing the Eulerian distance is straightforward and easy. In addition, for the sake of higher precision, we retain all POD modes, and we do not choose a threshold value for POD truncation either. Moreover, the first several modes are dominant, while the others are merely numerical noise with negligible amplitude (the corresponding $\alpha-$coordinates tend to zero). By consequence, their influence on the convergence criterion is fairly limited. To verify this, we performed a series of identifications by employing different number of modes (Table 4).

Table 4: Identified results with truncated POD modes.

Parameters	m=2	m=3	m=4	m=5	m=6
σ_y	245	108.0	106.0	105.8	106.0
n	0.175	0.321	0.326	0.326	0.326

We observe that the values of σ_y and n almost stabilized for $m \geq 4$. Thus, we would like to conclude that in order to identify material properties using the shape manifold learning approach, the size of minimum orthogonal basis of the reduced shape space is $m = 2l$, where l is the number of parameters. However, this is still open to discussion, and it is one of the reasons why we prefer using all the modes without truncation.

4.3.2. Sensitivity to different prescribed loads

In this section, we have tested our method with a prescribed force of 300N (instead of the previously used 500N). Due to the absence of experimental indentation data for this value, we first generated a pseudo imprint shape using the same simulation model and the pre-defined material parameter set: $\sigma_y = 107MPa, n = 0.324$. Next, a 3% random noise was introduced and finally, the 'missed' parameters were identified (results shown in Table 5).

As the table indicates, acceptable errors are obtained (lower than the percentage of introduced

Table 5: Identified results with prescribed force of 300N.

Parameters	Identified value	reference value	relative error
σ_y	109.7	107	2.52%
n	0.3208	0.324	0.99%

noise) when comparing with the pre-defined ones, and we may attribute this error to the inaccuracy of the manifold and noise introduced. However, it must be mentioned that, when using our method, the maximum force needs to be large enough to involve plastic deformations. Otherwise, imprint-based identification would be impossible since all the deformation would be recovered after elastic spring back.

4.3.3. Inaccuracy of local manifold

In the previous section, we mentioned that when we project the experimental imprint onto the shape space, *even* assuming that the indented material behaved exactly according to the postulated plastic hardening law, the projection will never lie *exactly* on the manifold due to noise in the measured data. While this statement is theoretically based on the fundamental hypothesis, and it is only true for the an "exact" manifold.

In the implementation of the current work, the local manifold is described by its parametric form using least squares approximation, and thus it is inexact. Consequently, the offset of experimental imprint from the local manifold may be attributed to two factors (assuming again that the indented material hardens according the power law):

1. inaccuracy of manifold;
2. measurement noise.

In order to quantify these two errors, we adopt the manifold in Fig.14, and project a smooth imprint simulated with the parameter set $\sigma_y = 107$ and $n = 0.324$ onto the $\alpha - space$. We obtain a distance of the projection to the manifold is 7.0×10^{-4}, compared with 3.0×10^{-3} for the imprint with noise. Thus, we may conclude that since the manifold is approximated in the vicinity of the snapshot, and considering the simplicity of the problem itself, the error caused by measurement error needs to be dominant compared with the error incurred by manifold inaccuracy. This statement could be further explained by observing the accuracy of identification using even lower-order polynomial basis in the next section.

4.3.4. The effect of polynomial basis

In present work, the higher-dimensional global manifold is approximated progressively by lower-dimensional local ones based on a set of snapshots in the vicinities of current evaluation point. A quadratic polynomial basis is adopted as it allows for gradient and Hessian evaluation. However, the number of terms of quadratic basis increases rapidly with the number of parameters. Therefore, we investigate a lower order bilinear basis for the sake of reduction in the number of snapshots per iteration. The essential significance of lower order polynomial basis will be firmly highlighted when more parameters need to be identified. For example, in the case where 5 parameters are involved, the number of snapshots per iteration needed for bilinear and quadratic basis is 16 and 32, respectively.

By choosing the same initial evaluation for the two parameters, a comparison of bilinear and quadratic basis are conducted and the results are given in Table.6. Excepting for the almost identical results, it is also observed that, as expected, the total numbers of simulations for bilinear basis is less than that for quadratic basis, 50 compared with 56.

Table 6: Identified results derived by adopting different polynomial basis.

Polynomial basis	σ_y	n	Iterations	Snapshots	Total simulations
Quadratic	107.0	0.324	8	7	56
Bilinear	108.4	0.321	10	5	50

4.3.5. The effect of number of snapshots M

In our fist test case on C100 steel, the local manifolds are approximated by a quadratic bivariate polynomial basis, in which 6 coefficients need to be determined. However, considering the numerical instability of simulation, we have chosen 7 snapshots to construct the local manifold so as to guarantee the unicity of solution to Eq.(13) in the case where one of the simulations does not converge.

To have a better understanding of the influence of the number of snapshots for each iteration, with the same specimen as in Section 4, we performed several identification procedures by adopting even more snapshots, and the stability can be observed form Table.7

Table 7: Identified results using different number of snapshots.

Parameters	$M = 7$	$M = 8$	$M = 9$	$M = 10$
σ_y	104.0	105.6	106.6	105.0
n	0.330	0.324	0.325	0.322

5. SECOND TEST CASE: AU4G aluminum alloy

Our first test-case involved a material (C100 steel) that exhibited a hardening behavior relatively close to that predicted by the Hollomon's power law. In addition, there was little noise in the imprint measurement. Both of these factors contributed to an accurate identification of the two power law parameters, since the numerical imprint assuming power law hardening differed by less than 4% from the experimental imprint with noise (Table.1-3).

While the first may not be the case each and every time we perform an indentation-based identification, it is a relatively simple matter to use a different or higher hardening law for conducting the FE simulations, since the order of the law and thus the number of parameters to be identified do not in any way change the application of the protocol. For the second issue, imprint measurement using our, and for that matter, *any* technique can generate noisy data despite taking every possible measure to minimize this.

In order to demonstrate the robustness of the proposed protocol, we now present a second test-case where the second of the above previously fulfilled criteria is not necessarily satisfied, i.e. noisy measurement of the indentation imprint. For this, we performed axisymmetric indentation on a specimen of the aluminium alloy AU4G (or AA2017) using a spherical tip indenter with a radius of 0.5 *mm* for two different maximum loads: 240KN and 360 KN. The elastic properties of this alloy are shown in Table.8.

The imprint was measured by chromatic confocal imaging with the Altisurf 500 machine used previously. Once again, we have used the 2 parameter Hollomon's power law with isotropic hardening to generate the simulated imprints. As mentioned in the previous section, the combined panning & zooming is the most reliable protocol for identification, thus the iteration histories derived from panning & zooming are listed in Table.9 and Table.10, considering two different experimental setups (maximum penetration force F_{max} equals to 240N and 360 respectively).

Table 8: Elastic properties for AU4G alloy and indenter used for the FE simulations.

Material properties	Specimen	Indenter
Young's moudulus	70GPa	600GPa
Poisson's ratio	0.33	0.23

Table 9: Iteration results for AU4G alloy ($F_{max} = 240N$).

Iter	σ_y	n	$\|\boldsymbol{\alpha}_{\text{exp}} - \boldsymbol{\alpha}^*\|$	ε_1	ε_2
1	300.00	0.250	0.0746	32.24%	32.59%
2	280.01	0.230	0.0532	23.02%	23.57%
3	260.03	0.210	0.0304	13.14%	14.12%
4	241.57	0.193	0.0060	2.60%	5.09%
5	239.70	0.192	0.0042	1.83%	4.90%
6	239.85	0.192	0.0040	1.72%	4.90%
7	241.57	0.193	0.0041	1.76%	4.88%
8	241.57	0.191	0.0039	1.67%	4.89%
9	240.52	0.190	0.0038	1.65%	4.90%
10	240.91	0.191	0.0043	1.86%	4.90%

Table 10: Iteration results for AU4G alloy ($F_{max} = 360N$).

Iter	σ_y	n	$\|\boldsymbol{\alpha}_{\text{exp}} - \boldsymbol{\alpha}^*\|$	ε_1	ε_2
1	300.00	0.250	0.1280	33.39%	33.95%
2	280.00	0.230	0.0898	23.41%	24.30%
3	260.01	0.210	0.0472	12.31%	13.22%
4	242.54	0.194	0.0050	1.29%	4.17%
5	253.25	0.180	0.0029	0.76%	4.01%
6	251.22	0.182	0.0036	0.95%	4.00%
7	251.72	0.183	0.0032	0.82%	4.00%
8	251.49	0.182	0.0022	0.57%	4.00%
9	251.49	0.182	0.0024	0.64%	4.00%
10	251.89	0.181	0.0026	0.67%	4.00%

A slight difference between the parameters identified for two different maximum force can be seen in the table. The reason should be resulted in the fact that the imprint profile for $F_{max} = 240N$ is measured with bigger noise: 4.90% compared with 4.00% obtained by $F_{max} = 360N$.
Besides, very similar identified results were obtained for the other two iteration algorithms. Thus, we consider our protocol as a stable method for identifying material plastic properties by considering only the imprint profile after an indentation test.

6. Conclusions and perspectives

In this paper, we propose a complete protocol for the identification of material work hardening properties, using only the imprint shape of an instrumented indentation test. By adopting the concept of the shape manifold, satisfactory results were obtained using a variety of algorithms. The main contributions may be listed as follows:

• The constructed α-manifold provides us a natural/physics-based way of smoothing the imprint data of a real experiment. This smoothing is based on the modes that capture the intrinsic features of imprint shapes governed by a given constitutive law. This approach also allows us to directly compare the imprints obtained by FE simulation (in the inverse analysis) with those obtained by actual indentation on the sample specimens.

• Almost identical power law work hardening parameter sets (σ_y, n) are obtained with different convergence algorithms even when starting from very different initial points. The error between the experimental imprint and simulated imprint with identified parameters can be controlled to a considerably low level, around 1%.

Though, our protocol can and should be improved in order to reuse the imprints in the current iteration when they are situated in the design window of next iteration, as this will yield a significant reduction in computation time. Besides, we may also study the possibility of our protocol for anisotropic materials and sharp indenters in our next work. From the methodological point of view, further comparisons should be done with Isomap or Locally Linear Embedding methods.

Acknowledgements

This work was carried out in the framework of the Labex MS2T, which was funded by the French Government, through the program "Investments for the future" managed by the National Agency for Research (Reference ANR-11-IDEX-0004-02). This work is also funded by the China Scholarship Council (CSC).

References

[1] B. W. Mott, Micro-indentation hardness testing, Butterworths Scientific Publications, 1956.
[2] D. Tabor, The hardness of metals, Vol. 10, ClarendonP, 1951.
[3] S. Kamali-Bernard, D. Keinde, F. Bernard, Effect of aggregate type on the concrete matrix/aggregates interface and its influence on the overall mechanical behavior. a numerical study, Key Engineering Materials 617 (2014) 14 – 17.
[4] C. K. Moy, M. Bocciarelli, S. P. Ringer, G. Ranzi, Identification of the material properties of al 2024 alloy by means of inverse analysis and indentation tests, Materials Science and Engineering: A 529 (2011) 119–130.
[5] R. C. Paietta, S. E. Campbell, V. L. Ferguson, Influences of spherical tip radius, contact depth, and contact area on nanoindentation properties of bone, Journal of biomechanics 44 (2) (2011) 285–290.
[6] R. F. Gibson, A review of recent research on nanoindentation of polymer composites and their constituents, Composites Science and Technology 105 (2014) 51–65.
[7] C. Moussa, X. Hernot, O. Bartier, G. Delattre, G. Mauvoisin, Identification of the hardening law of materials with spherical indentation using the average representative strain for several penetration depths, Materials Science and Engineering: A 606 (2014) 409–416.

[8] C. Moussa, O. Bartier, G. Mauvoisin, X. Hernot, J.-M. Collin, G. Delattre, Experimental and numerical investigation on carbonitrided steel characterization with spherical indentation, Surface and Coatings Technology 258 (0) (2014) 782 – 789.
[9] A. Giannakopoulos, S. Suresh, Determination of elastoplastic properties by instrumented sharp indentation, Scripta materialia 40 (10) (1999) 1191–1198.
[10] T. Nakamura, T. Wang, S. Sampath, Determination of properties of graded materials by inverse analysis and instrumented indentation, Acta Materialia 48 (17) (2000) 4293–4306.
[11] T. Venkatesh, K. Van Vliet, A. Giannakopoulos, S. Suresh, Determination of elasto-plastic properties by instrumented sharp indentation: guidelines for property extraction, Scripta materialia 42 (9) (2000) 833–839.
[12] T. Capehart, Y. Cheng, Determining constitutive models from conical indentation: Sensitivity analysis, Journal of materials research 18 (04) (2003) 827–832.
[13] X. Chen, J. J. Vlassak, Numerical study on the measurement of thin film mechanical properties by means of nanoindentation, Journal of Materials Research 16 (10) (2001) 2974–2982.
[14] J. Alkorta, J. Martinez-Esnaola, J. G. Sevillano, Absence of one-to-one correspondence between elastoplastic properties and sharp-indentation load–penetration data, Journal of materials research 20 (02) (2005) 432–437.
[15] J. Alcala, A. Barone, M. Anglada, The influence of plastic hardening on surface deformation modes around vickers and spherical indents, Acta Materialia 48 (13) (2000) 3451 – 3464.
[16] B. Taljat, G. Pharr, Development of pile-up during spherical indentation of elasticplastic solids, International Journal of Solids and Structures 41 (14) (2004) 3891 – 3904.
[17] R. Mulford, R. J. Asaro, R. J. Sebring, Spherical indentation of ductile power law materials, Journal of Materials Research 19 (2004) 2641–2649.
[18] C. Moy, M. Bocciarelli, S. Ringer, G. Ranzi, Indentation and imprint mapping for the identification of material properties in multi-layered systems, Computational Materials Science 50 (5) (2011) 1681 – 1691.
[19] K. Matsuda, Prediction of stress-strain curves of elastic-plastic materials based on the vickers indentation, Philosophical Magazine A 82 (10) (2002) 1941–1951.
[20] M. Bocciarelli, V. Buljak, C. Moy, S. Ringer, G. Ranzi, An inverse analysis approach based on a {POD} direct model for the mechanical characterization of metallic materials, Computational Materials Science 95 (0) (2014) 302 – 308.
[21] M. Bocciarelli, G. Bolzon, Indentation and imprint mapping for the identification of constitutive parameters of thin layers on substrate: perfectly bonded interfaces, Materials Science and Engineering: A 448 (1) (2007) 303–314.
[22] M. Bocciarelli, G. Maier, Indentation and imprint mapping method for identification of residual stresses, Computational Materials Science 39 (2) (2007) 381–392.
[23] O. Bartier, X. Hernot, G. Mauvoisin, Theoretical and experimental analysis of contact radius for spherical indentation, Mechanics of Materials 42 (6) (2010) 640 – 656.
[24] C. Ullner, E. Reimann, H. Kohlhoff, A. Subaric-Leitis, Effect and measurement of the machine compliance in the macro range of instrumented indentation test, Measurement 43 (2) (2010) 216 – 222.
[25] S.-K. Kang, Y.-C. Kim, Y.-H. Lee, J.-Y. Kim, D. Kwon, Determining effective radius and frame compliance in spherical nanoindentation, Materials Science and Engineering: A 538 (0) (2012) 58 – 62.
[26] J. Bressan, A. Tramontin, C. Rosa, Modeling of nanoindentation of bulk and thin film by finite element method, Wear 258 (1) (2005) 115–122.
[27] K.-D. Bouzakis, N. Michailidis, S. Hadjiyiannis, G. Skordaris, G. Erkens, The effect of specimen roughness and indenter tip geometry on the determination accuracy of thin hard coatings stress–strain laws by nanoindentation, Materials characterization 49 (2) (2002) 149–156.
[28] M. Lichinchi, C. Lenardi, J. Haupt, R. Vitali, Simulation of berkovich nanoindentation experiments on thin films using finite element method, Thin solid films 312 (1) (1998) 240–248.
[29] K. J. Van Vliet, L. Prchlik, J. F. Smith, Direct measurement of indentation frame compliance, Journal of Materials Research 19 (2004) 325–331.
[30] P. Grau, G. Berg, W. Fraenzel, H. Meinhard, Recording hardness testing. problems of measurement at small indentation depths, physica status solidi (a) 146 (1) (1994) 537–548.
[31] P. Brammer, O. Bartier, X. Hernot, G. Mauvoisin, S.-S. Sablin, An alternative to the determination of the effec-

tive zero point in instrumented indentation: use of the slope of the indentation curve at indentation load values, Materials & Design 40 (2012) 356–363.
[32] Y. Liu, B. Wang, M. Yoshino, S. Roy, H. Lu, R. Komanduri, Combined numerical simulation and nanoindentation for determining mechanical properties of single crystal copper at mesoscale, Journal of the Mechanics and Physics of Solids 53 (12) (2005) 2718–2741.
[33] G. Berkooz, P. Holmes, J. L. Lumley, The proper orthogonal decomposition in the analysis of turbulent flows, Annual Rev. Fluid Mech (1993) 539–575.
[34] B. Raghavan, M. Hamdaoui, M. Xiao, P. Breitkopf, P. Villon, A bi-level meta-modeling approach for structural optimization using modified {POD} bases and diffuse approximation, Computers & Structures 127 (0) (2013) 19 – 28.
[35] B. Raghavan, L. Xia, P. Breitkopf, A. Rassineux, P. Villon, Towards simultaneous reduction of both input and output spaces for interactive simulation-based structural design, Computer Methods in Applied Mechanics and Engineering 265 (2013) 174–185.
[36] D. Millan, M. Arroyo, Nonlinear manifold learning for model reduction in finite elastodynamics, Computer Methods in Applied Mechanics and Engineering 261-262 (0) (2013) 118 – 131.
[37] D. Millan, A. Rosolen, M. Arroyo, Nonlinear manifold learning for meshfree finite deformation thin-shell analysis, International Journal for Numerical Methods in Engineering 93 (7) (2013) 685–713.
[38] G. Le Quilliec, B. Raghavan, P. Breitkopf, A manifold learning-based reduced order model for springback shape characterization and optimization in sheet metal forming, Computer Methods in Applied Mechanics and Engineering 285 (2015) 621–638.
[39] B. Raghavan, G. Le Quilliec, P. Breitkopf, A. Rassineux, J.-M. Roelandt, P. Villon, Numerical assessment of springback for the deep drawing process by level set interpolation using shape manifolds, International Journal of Material Forming 7 (4) (2014) 487–501.
[40] B. Raghavan, M. Xiao, P. Breitkopf, P. Villon, Implicit constraint handling for shape optimisation with pod-morphing, European Journal of Computational Mechanics 21 (3-6) (2012) 325–336.
[41] G. H. Golub, C. Reinsch, Singular value decomposition and least squares solutions, Numerische mathematik 14 (5) (1970) 403–420.
[42] Y.-T. Cheng, C.-M. Cheng, Scaling, dimensional analysis, and indentation measurements, Materials Science and Engineering: R: Reports 44 (4) (2004) 91–149.
[43] M. F. Ashby, D. Cebon, Materials selection in mechanical design, Le Journal de Physique IV 3 (C7) (1993) C7–1.
[44] D. Hibbitt, B. Karlsson, P. Sorensen, Abaqus analysis users manual, Pawtucket, USA.